PASJ: Publ. Astron. Soc. Japan , 1–??,

Suzaku discovery of iron absorption lines in outburst spectra of the X-ray transient 4U 1630 − 472

Aya Kubota[1], Tadayasu Dotani[2], Jean Cottam[3], Taro Kotani[4], Chris Done[2,5], Yoshihiro Ueda[6], Andrew C. Fabian[7], Tomonori Yasuda[8], Hiromitsu Takahashi[8], Yasushi Fukazawa[8], Kazutaka Yamaoka[9], Kazuo Makishima[1,10], Shinya Yamada[10], Takayoshi Kohmura[11], and Lorella Angelini[3]

[1] *Institute of Physical and Chemical Research (RIKEN), 2-1 Hirosawa, Wako, Saitama 351-0198*
aya@crab.riken.jp

[2] *Institute of Space and Astronautical Science, Japan Aerospace Exploration Agency, 3-1-1 Yoshinodai, Sagamihara, Kanagawa 229-8510*

[3] *Exploration of the Universe Division, NASA Goddard Space Flight Center, Greenbelt, MD 20771, USA*

[4] *Department of Physics, Tokyo Tech, 2-12-1 O-okayama, Meguro, Tokyo 152-8551*

[5] *Department of Physics, University of Durham, South Road, Durham, DH1 3LE, UK*

[6] *Department of Astronomy, Kyoto University, Sakyo-ku, Kyoto 606-8502*

[7] *Institute of Astronomy, Madingley Road, Cambridge CB3 0HA, UK*

[8] *Department of Physics, Hiroshima University, 1-3-1 Kagamiyama, Higashi-Hiroshima, Hiroshima 739-8526*

[9] *Department of Physics, Aoyama Gakuin University, Sagamihara, Kanagawa 229-8558*

[10] *Department of Physics, University of Tokyo, 7-3-1 Hongo, Bunkyo-ku, Tokyo 113-0033*

[11] *Physics Department, Kogakuin University 2665-1, Nakano-cho, Hachioji, Tokyo, 192-0015*

(Received 2006 July 25; accepted 2006 October 12)

Abstract

We present the results of six Suzaku observations of the recurrent black hole transient 4U 1630 − 472 during its decline from outburst from February 8 to March 23 in 2006. All observations show the typical high/soft state spectral shape in the 2–50 keV band, roughly described by an optically thick disk spectrum in the soft energy band plus a weak power-law tail that becomes dominant only above ∼20 keV. The disk temperature decreases from 1.4 keV to 1.2 keV as the flux decreases by a factor 2, consistent with a constant radius as expected for disk-dominated spectra. All the observations reveal significant absorption lines from highly ionized (H-like and He-like) iron Kα at 7.0 keV and 6.7 keV. The brightest datasets also show significant but weaker absorption structures between 7.8 keV and 8.2 keV, which we identify as a blend of iron Kβ and nickel Kα absorption lines. The energies of these absorption lines suggest a blue shift with an outflow velocity of ~ 1000 km s^{-1}. The H–like iron Kα equivalent width remains approximately constant at ~ 30 eV over all the observations, while that of the He–like Kα line increases from 7 eV to 20 eV. Thus the ionization state of the material decreases, as expected from the decline in flux. We fit the profiles with Voigt functions (curve of growth) to derive absorbing columns, then use these together with detailed photo-ionization calculations to derive physical parameters of the absorbing material. The data then constrain the velocity dispersion of the absorber to 200–2000 km s^{-1}, and the size of the plasma as $\sim 10^{10}$ cm assuming a source distance of 10 kpc.

Key words: accretion, accretion disks — X-rays: individual (4U 1630 − 472)

1. Introduction

In recent years, a growing number of X-ray binaries have been found to exhibit absorption lines from highly ionized elements (e.g., Boirin et al. 2004 and references therein; Church et al. 2005). These systems range from microquasars such as GRO J1655−40 (Ueda et al. 1998; Yamaoka et al. 2001; Miller et al. 2006) and GRS 1915+105 (Kotani et al. 2000; Lee et al. 2002) to low-mass X-ray binaries such as GX 13+1 (Ueda et al. 2001; Sidoli et al. 2002), X 1658−298 (Sidoli et al. 2001) and X 1254−690 (Boirin & Parmar 2003). These systems are viewed at high inclination angles, and the absorption structure is visible throughout the orbital period (e.g. Yamaoka et al. 2001; Sidoli et al. 2001; 2002). The absorption features are therefore thought to originate in material that is associated with and extends above the outer accretion disk. This is illuminated by the X-rays produced from the innermost regions of the accretion flow (both the disk and hard X-ray coronal emission). The reprocessed emission and scattered flux from the extended wind can be seen directly in the Accretion Disk Corona sources, where the intrinsic X-rays are obscured (e.g. Kallman et al. 2003), but for the majority of highly inclined sources, the wind

material is seen in absorption against the much brighter intrinsic central X-ray source. Multiple absorption lines seen there then give an excellent probe of the physical conditions in the wind (e.g. Ueda et al. 2004; Miller et al. 2006), where the spectra indicate the presence of significant amounts of highly ionized outflowing material. Such accretion disk winds can be produced by thermal driving (e.g., Begelman et al. 1983), and/or by magnetic forces (Blandford & Payne 1982) as inferred by Miller et al. (2006) from Chandra HETGS data of GRO J1655−40.

4U 1630−472 is a black hole candidate (e.g., Tanaka & Lewin 1995; McClintock & Remillard 2003), known for X-ray outbursts that repeat with an interval of roughly 600–690 days (Jones et al. 1976; Parmar, Angelini & White 1995). The source has been observed with every major mission from EXOSAT (Kuulkers et al. 1997; Parmar et al. 1986), Ginga (Parmar et al. 1997), BATSE CGRO (Bloser et al. 1996), to Beppo-SAX (Oosterbroek et al. 1998), RXTE (Tomsick et al. 1998; Kuulkers et al. 1998; Hjellming et al. 1999; Cui et al. 2000; Dieters et al. 2000; Trudolyubov et al. 2001; Kalemci et al. 2004; Abe et al. 2005), ASCA (Abe et al. 2005), and recently Chandra (J. Miller, private communication). These X-ray observations showed that the source is absorbed heavily with $N_{\rm H} = (5\text{–}12) \times 10^{22}$ cm^{-2} (Tomsick et al. 1998; Kuulkers et al. 1997; Cui et al. 2000; Trudolyubov et al. 2001; Abe et al. 2005). While the IR counterpart was found during a 1998 outburst by Augusteijn et al. (2001), no optical counterpart is known for 4U 1630−472, most likely due to its high reddening and location in a crowded star field (Parmar, Stella & White 1986). Thus, the distance, inclination angle, and mass of the compact object are unknown for 4U 1630−472. This source is classified as a black hole not from dynamic mass measurements, but because of the similarity of its X-ray spectral and timing properties to those of systems with measured black hole masses.

This source was observed six times with Suzaku during its most recent outburst as part of a program to study discrete spectral structures as a function of the changing accretion conditions. The Suzaku monitoring observation led to successful detection of absorption lines on all occasions. Though one of the absorption lines may have been detected by Chandra (J. Miller, private communication), the Suzaku XIS data reveal the line with a much higher significance, thanks to its larger effective area at 7 keV than that of Chandra. In this paper, we focus mainly on the absorption line structures, and how these discrete features evolve over the two months span of our observations. Considering the large absorption column density, we assume the source distance, D, at 10 kpc in this paper. In addition, by comparison to the other black hole binaries reported to show absorption lines, an inclination angle, i, of 70° is assumed. Errors quoted in this paper represent 90% confidence limit for a single parameter unless otherwise specified.

2. Observations and data reduction

2.1. Observations

An outburst of 4U 1630 − 472 was reported by the RXTE All Sky Monitor (ASM; Levine et al. 1996) on 2005 December. From 2006 February 8 through March 23, we observed the source six times with a series of 21–23 ks exposures as part of the initial performance verification of Suzaku. Suzaku is the 5th X-ray astronomy satellite of Japan launched on July 10, 2005, with an M-V rocket from the Uchinoura space center (Mitsuda et al. 2006). It carries 4 sets of X-ray telescopes (Serlemitsos et al. 2006) each with a focal-plane X-ray CCD camera (XIS, X-ray Imaging Spectrometer; Koyama et al. 2006) operating in the energy range of 0.2–12 keV, together with a non-imaging Hard X-ray Detector (HXD, Takahashi et al. 2006), which covers the 10–600 keV energy band with Si PIN photo-diodes and GSO scintillation counters. Three of the XIS (XIS0, 2, 3) have front-illuminated (FI) CCDs, while XIS1 utilizes a back-illuminated (BI) CCD, achieving an improved soft X-ray response but poorer hard X-ray sensitivity. Considering the large column density to 4U 1630−472, we concentrate on the harder X-ray band in this paper, and only analyze the data from the FI CCDs.

Figure 1 shows a lightcurve of 4U 1630 − 472 obtained by the RXTE ASM. The Suzaku observations are indicated with downward arrows. Because the optical axes of the XIS and the HXD are slightly offset, the source was put at the center of the HXD field of view during the observations, to maximize the HXD count rate, and to reduce the XIS count rate as pileup is an issue for such a bright source (see below). The HXD was operated in the nominal mode throughout the observations. Because the source was very bright, the XIS was operated with the 1/4 window option, in which a smaller field of view of $17'.8 \times 4'.5$ is read out every 2 s. A burst option was added in the first four observations. This decreases the effective exposure by a factor of two. The editing modes of the FI CCDs (XIS023) were set to 3×3 and 2×2 for high and medium data rates, respectively. Table 1 summarizes the details of the observations.

2.2. Data reduction

For both the XIS and the HXD, we use version 0.7 screened data provided by the Suzaku team. The screening of the version 0.7 XIS data are based on the following standard criteria: a) Only GRADE0, 2, 3, 4, 6 events are accumulated, b) The time interval after passage through the South Atlantic Anomaly is larger than 436 seconds, c) The object is at least 5° and 20° above the rim of the Earth during night and day, respectively. We limit our analysis to the 3×3 mode data (high data rate), because the 2×2 mode data (medium data rate) are not well calibrated at this time. During the 2nd and 5th observations, more than half of the exposure was acquired in 2×2 mode, and thus these data have poorer statistics. The exposure times for the total and high data rate are summarized in Table 1.

The XIS events were extracted from a circular region

Table 1. Suzaku Observations of 4U 1630 − 472

Epoch	Start	End	XIS options	Exposure [ks] *		Flux [erg s^{-1} cm^{-2}]	
				total†	High†	2–10 keV	20–40 keV
1	Feb 8 8:14	Feb 9 3:20	1/4 window, 1-s burst	22.2	22.2	4.6×10^{-9}	6.9×10^{-11}
2	Feb 15 23:08	Feb 16 13:08	1/4 window, 1-s burst	21.5	9.6	4.0×10^{-9}	6.7×10^{-11}
3	Feb 28 23:00	Mar 1 16:43	1/4 window, 1-s burst	21.3	21.3	3.1×10^{-9}	5.0×10^{-11}
4	Mar 8 01:39	Mar 8 17:31	1/4 window, 1-s burst	21.2	20.7	2.8×10^{-9}	3.5×10^{-11}
5	Mar 15 5:19	Mar 15 17:51	1/4 window	23.2	5.2	2.5×10^{-9}	2.6×10^{-11}
6	Mar 23 9:57	Mar 23 22:21	1/4 window	21.7	15.4	2.2×10^{-9}	1.5×10^{-11}

* Without correction for the burst option. With the burst option, the net exposure is a half of the nominal exposure listed in this table.
† Net exposures of total (medium and high data rates) and only high data rate are shown. For FI-CCDs, observations were performed with 3×3 and 2×2 mode in data-rate High and Med, respectively.

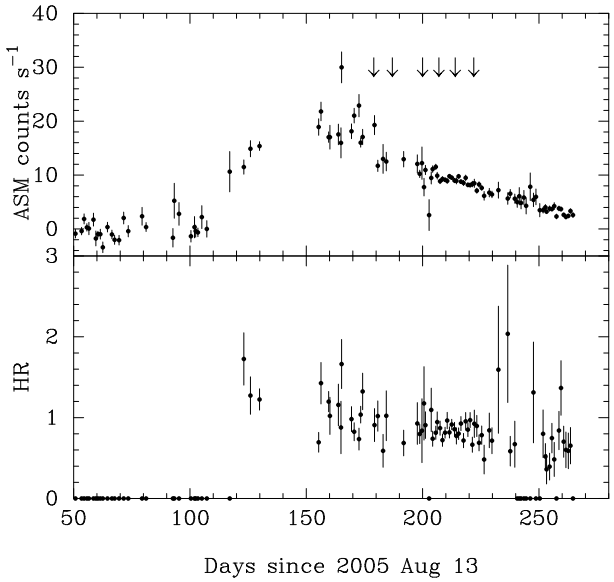

Fig. 1. The 1.5–12 keV light curve of 4U 1630 − 472 (top panel), and hardness ratio of 5–12 keV to 3–5 keV (bottom panel),obtained with the RXTE ASM since 2005 August 13 (MJD 53595). The Suzaku observations are indicated with down-arrows.

with a radius of 4′.3 centered on the image peak. This extraction circle is larger than the window size. The effective extraction region is therefore the intersection of the window and this circle. The background was entirely negligible throughout the six observations (less than 1% of the signal at 9 keV), so was not subtracted from the data. Using XIS2 as a reference, we find that the 2–10 keV count rate declined over the six observations, with 124, 112, 90, 82, 74, and 64 cts s^{-1} respectively, roughly corresponding to 4.6, 4.0, 3.1, 2.8, 2.5, and 2.2×10^{-9} erg s^{-1} cm^{-2} in the same energy band. Within each observation, we find no significant intensity variation intrinsic to the source.

The source was so bright during these observations that the XIS suffered from photon pileup at the image center. A rough threshold above which the photon pileup becomes significant is ∼100 cts exposure^{-1} for a point source. The count rates of 4U 1630 − 472 during the observations were around this level. Furthermore, because 4U 1630 − 472 has a very soft energy spectrum, the effect of photon pileup can be significant in the hard band spectra. Therefore, we excluded a circular region of 30″ at the image center from the event extraction region to minimize these effects. This did not remove the photon pileup completely, and an artificial structure is seen as a hard excess above ∼ 8 keV at the <5–10% level. Because photon pileup tends to produce X-ray events which have twice (or a little more) as high an energy as the most abundant events (in this case, about 4 keV), we modeled the artificial structure as a gaussian centered at 10 keV with a fixed width of $\sigma =$ 1 keV. As seen in the next section, this phenomenological model works quite well to compensate for the effect of pileup.

Because the event extraction region has a complex shape (an annulus truncated with the window size), we calculated the effective area for each XIS sensor by using XISSIMARFGEN (version 2006-04-24), which calculates the arf file through Monte Carlo simulations. The three FI CCDs have almost the same performance, so we have added their data to increase the statistics in the spectra. Hereafter we refer to the summed data as XIS023. We calculated the corresponding instrumental responses by summing the latest redistribution matrices of ae_xi[0,2,3]_20060213.rmf using the FTOOL ADDRMF and the ARF files using the FTOOL ADDARF.

Though the main objective of this paper is the absorption structure in the XIS energy band, it is also useful to understand the continuum emission since this provides a knowledge of spectral states and photoionising flux. We thus analyzed the HXD data using only the PIN data, since the source is dim in the GSO band. Both high and medium data rate are used in the PIN data analysis. The version 0.7 PIN data are screened by the following selection criteria: a) The object is at least 5° above the earth rim, b) The time interval after passage through the South Atlantic Anomaly is longer than 500 seconds, c) The cutoff rigidity is greater than 8 GeV c^{-1}. The PIN background events were provided by the HXD team for each observation based on two different models, A and B (Kokubun et al. 2006). Here we constructed the PIN background spectra based on model B filtered by the same good time intervals. The latest version of the response

matrix, ae_hxd_pinhxnom_20060419.rmf, was used in our spectral analysis. Even if we allow 5% systematic uncertainty in the background level, the source is clearly detected up to 40 keV and 35 keV in PIN data from the first four and last two observations, respectively. Dead time fractions were calculated from the pseudo event rates (Takahashi et al. 2006; Kokubun et al. 2006) as 5.3, 4.3, 4.6, 5.1, 4.6, and 4.6%, in the first to last observations, respectively. After the dead time correction, the background subtracted PIN count rates are estimated to be 0.16, 0.13, 0.093, 0.065, 0.055, and 0.043 cts s^{-1} in the range of 20–40 keV, corresponding to 6.9, 6.7, 5.0, 3.5, 2.6, and 1.5×10^{-11} erg s^{-1} cm^{-2}.

2.3. Calibration uncertainties of the XIS data

Because the XIS calibration is still in progress, we include a brief description of the calibration uncertainties. The XIS energy scale is relatively well calibrated with an uncertainty of less than 5 eV, or 0.2% when the standard mode is used (Koyama et al. 2006). However, when a window option is applied, the gain can change slightly, because the number of frame-store and parallel transfers are different than in the standard mode. This difference is not taken into account in the version 0.7 processing software. Since a window option was used for all the observations of 4U $1630-472$, the XIS instrument team estimates that this produces a systematic gain difference of $\sim$10 eV at 6 keV at the time of 4U $1630-472$ observations. When the window option is used, the onboard ^{55}Fe calibration source is not directly visible but some events can be scattered into the active window in XIS2, which has the strongest calibration sources. The scattered ^{55}Fe events are accumulated from the regions free from the source photons (1/8 of the window area for each side). We obtain an average energy of 5891 ± 20 eV. This is consistent with the $\sim$10 eV offset estimated above. We also examined the data for a possible gain shift due to the large surface brightness (local event density) of the image, by comparing the absorption line energies in the observed spectra for different radii of extraction annuli. We find no significant differences. Thus a conservative estimate is that the XIS gain at the iron band is correct to within 20 eV during the 4U $1630-472$ observations.

The energy resolution of the XIS is gradually degrading due to the radiation damage on the CCD. However, this effect is not yet included in the currently available response matrices. At the time of the 4U $1630-472$ observations, a narrow line at 6 keV would appear broadened with $\sigma \sim 40$ eV, where σ is an equivalent gaussian width (standard deviation). Thus, when we evaluate a line width, we take this effect into account. It is important to note that this does not affect the measurement of the equivalent width.

The effective areas of the XIS and PIN are calibrated using observations of the Crab Nebula. The accuracy is expected to be 5–10%. This is sufficient to estimate various emission parameters of 4U $1630-472$. However, because of the very good statistics of the data, the systematic errors in calibration could degrade the model fitting significantly. A major contribution to the systematic error is the calibration uncertainty at gold M-II edge in the instrumental response. To account for this residual, we added a gaussian at ~ 3.2 keV with a fixed width of $\sigma = 0.1$ keV.

3. Analyses and results

3.1. Broad band features

Figure 2a shows the 2–50 keV spectra of 4U $1630-472$ obtained with the XIS023 and the PIN. We do not use data below 2 keV, because of large interstellar absorption. An instrument-independent way to view the spectra is to construct the ratio of the source spectra to the corresponding data from the Crab Nebula, which has an approximately power-law spectrum with $\Gamma = 2.1$, and interstellar absorption of $N_{\rm H} = 3 \times 10^{21}$ cm^{-2} (Toor & Seward 1974; Schattenburg & Canizares 1986). Figure 2b shows the Crab ratios calculated using the Crab data obtained with Suzaku on 2006 April 5 at the HXD nominal position and the XIS operated with the 1/4 window option. This plot reveals several noticeable features in the broad band source spectra. The source spectra are characterized by a dominant soft thermal component in the XIS band, which is heavily absorbed, while the harder X-ray PIN data clearly show a weak power-law tail.

The dominant soft component is generally observed from bright black hole binaries in the high/soft state (Tanaka & Lewin 1995), and is believed to be emission from the optically thick standard accretion disk (Shakura & Sunyaev 1973). In the Crab ratio (figure 2b), the weak power-law tail is roughly characterized as $\Gamma \sim 2$ in the first two observations. When the 20–50 keV PIN spectra of these two observations are fitted with the single power-law model under the current response matrix, the values of Γ are obtained as 2.4 ± 0.4 and 2.5 ± 0.5, respectively. The extrapolated 20–100 keV fluxes are estimated as $(1.4 \pm 0.3) \times 10^{-10}$ and $(1.1 \pm 0.3) \times 10^{-10}$ erg s^{-1} cm^{-2}, respectively, which are only 3 % of the absorbed disk flux in the range of 2–10 keV. Though the steeper power-law tails may be suggested on the latter four observations from the Crab ratio plot (figure 2b), they are difficult to quantify because of their faintness under the current background uncertainty. Further detailed analysis of the HXD data will be presented in a separate paper.

The dominance of the disk and the weak power-law tail are both characteristic of the high/soft state. In addition, the Crab ratios also reveal the presence of complex absorption structures in the iron K band. In this paper, we concentrate on these absorption line structures and their relation to the accretion disk parameters. Hereafter, we perform detailed spectral analyses on the XIS data.

3.2. XIS spectra with canonical multi-color disk and negative gaussian fits

Figure 3 shows the 2–10 keV XIS raw spectra. To reproduce the continuum spectra, we use the multi-color disk model (DISKBB in XSPEC[1], Mitsuda et al. 1984; Makishima

[1] http://heasarc.gsfc.nasa.gov/docs/xanadu/

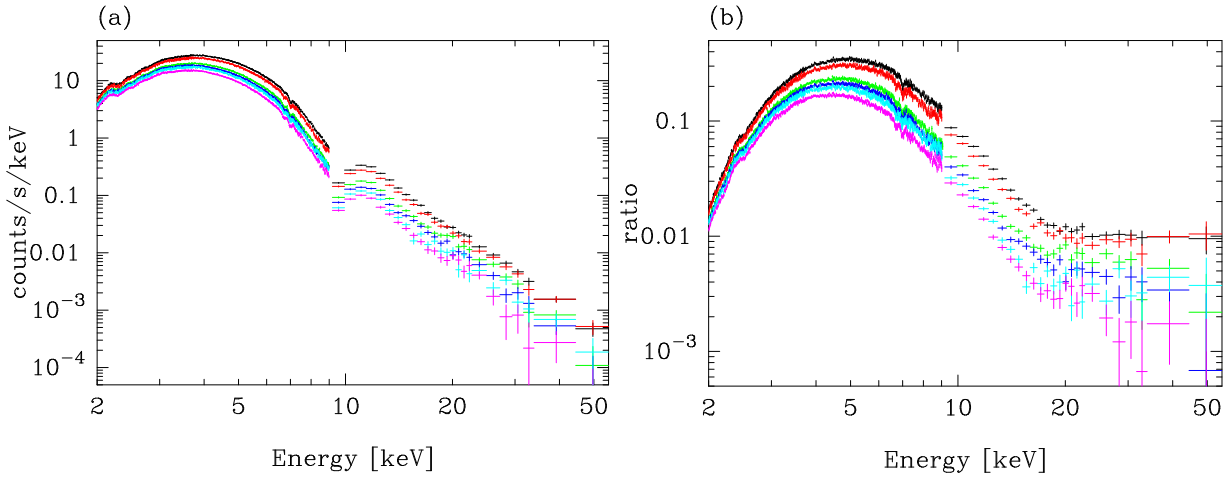

Fig. 2. (a) The X-ray spectra of 4U 1630 − 472 obtained with the XIS023 and the HXD PIN. The first to the last observations are shown with different colors as black, red, green, blue, right blue, and magenta. (b) The ratio of 4U 1630 − 472 spectra to the Crab spectrum.

et al. 1986) modified by interstellar absorption (WABS model; Morrison & McCammon 1983), following the canonical modeling for the high/soft state black hole binaries. Here, the DISKBB model approximates emission from the standard accretion disk, and is known to successfully reproduce the dominant soft spectra of the high/soft state black holes. As shown in figure 2b, the contribution of the power-law tail is negligible in the XIS energy band, so is not included in the spectral fitting. The residual effects of pileup are modeled by a broad gaussian at 10 keV (see § 2.2), and the current uncertainties in the instrument response at the gold M-II edge by another gaussian at 3.2 keV (see § 2.3).

We start with the first observation, which showed the brightest spectrum. The continuum is well reproduced by the DISKBB model with a disk temperature of $kT_{\rm in} = 1.39$ keV. This is amongst the highest disk temperatures observed with RXTE from this source in previous high/soft states (e.g., Abe et al. 2005). A disk bolometric luminosity of $L_{\rm disk} = 2.8 \times 10^{38} \cdot a$ erg s^{-1} and an apparent disk inner radius of $r_{\rm in} = 24 \cdot \sqrt{a}$ km are obtained, where a is defined as $(D/10\ {\rm kpc})^2/(\cos i/\cos 70^\circ)$. The absorbing column density, $N_{\rm H}$, is estimated to be 8.15×10^{22} cm^{-2}. This is close to that seen with previous observations by ASCA and RXTE (e.g., Abe et al. 2005).

The fit with this simple model is however far from acceptable ($\chi^2/dof = 1465.0/574$) because of the complex structure in the iron K band. Residuals between the data and the best-fit continuum model are shown in the middle panel of figure 3a. The most obvious features are two narrow dips at 7.0 keV and 6.8 keV. We therefore add two negative gaussians to the model. The fit is dramatically improved with $\chi^2/dof = 714.0/570$. The line center energies are estimated to be $7.001^{+0.006}_{-0.005}$ keV and 6.73 ± 0.02 keV, consistent with the H-like and He-like iron Kα lines at 6.966 keV and 6.697 keV [2]; the lines are possibly blue-shifted with $z \sim 5 \times 10^{-3}$. The equivalent widths are 30 eV and 7 eV, for the H-like and He-like lines, respectively. The lines are narrow with an upper limit to σ of 40 eV and 50 eV. These values are consistent with what we expect for narrow lines given the current response matrix, which does not include the degradation of the energy resolution (§ 2.3). We thus fix the value of σ at 10 eV to represent intrinsically narrow lines in this subsection.

In addition to these obvious line structures, the residuals reveal weaker absorption structures at 7.8 keV and 8.2 keV. These energies are very similar to the rest frame energies of He-like and H-like iron Kβ lines, namely 7.88 keV and 8.25 keV. However, they are also close in energy to the He-like and H-like nickel Kα lines at 7.80 keV and 8.09 keV, respectively, which can have comparable equivalent width to that of the iron Kβ lines (Kotani et al 2000). The data can marginally constrain two weak lines at these energies, but not four. Hence we include two additional negative gaussians, again with the width σ fixed at 10 eV, and allow the energies to vary freely. This decreases χ^2/dof to 686.4/566, indicating that the two negative gaussians are statistically significant at the 99.98% confidence level using an F-test (where $F(\nu, \Delta\nu) \equiv (\Delta\chi^2/\Delta\nu)/\chi^2_\nu = 5.65$). The best-fit parameters are summarized in Table 2. Residuals between the data and the best-fit model are shown in the bottom panel in figure 3a. The inferred energies are almost consistent with H-like and He-like iron Kβ, though they can be contaminated by nickel Kα.

We performed the same spectral analysis on the other five observations. The XIS spectra, the best-fit models, and the residuals are shown in figure 3b–f. The best-fit continuum and absorption parameters are summarized in Table 2, and the time histories of the continuum parameters are given in figure 4. Through the six observations over two months, the value of $r_{\rm in}$ remained approx-

[2] Weighted averages of Kα_1 and Kα_2 by referring to the National Institute of Standards and Technology (NIST; see http://aeldata.phy.nist.gov/archive/data.html) and Drake (1988) for H-like and He-like Kα, respectively.

imately constant at $25 \cdot \sqrt{a}$ km, while the disk temperature gradually decreased to 1.18 keV, corresponding to a factor 1.75 decrease in the disk bolometric luminosity to $L_{\rm disk} = 1.6 \times 10^{38} \cdot a$ erg s^{-1}. The constancy of $r_{\rm in}$ is another characteristic feature of the high/soft state of black hole binaries (e.g., Tanaka & Lewin 1995 and references therein), and confirms that the object was indeed in the high/soft state. The correlated decrease in the derived value of $N_{\rm H}$ by $\sim$3% could be an artifact of the over-simplified DISKBB model; it assumes that the disk radiates locally as a blackbody, but distortions from this are suggested both observationally (e.g., Kubota & Makishima 2004; Abe et al. 2005) and theoretically (Watarai et al. 2000; Davis et al. 2005) from such luminous binaries.

Irrespective of the continuum modeling, the two strong iron Kα lines are clearly detected throughout the observations, whereas the weaker lines at higher energies are significantly detected in the first four datasets (F-test significance values are given in Table 2). Figure 5 shows an enlargement of the 6–9 keV spectra, and residuals between the data and the continuum model. The time histories of the individual absorption-line equivalent widths and their energies are plotted in figure 6. While the equivalent width of the H-like line was almost constant throughout the observations, that of the He-like line increased by a factor of two between the first and second observations, and then perhaps increased slightly more through the subsequent observations. These imply that the ionization state of the absorbing gas decreased over time, as expected from the declining source luminosity.

The time averaged center energies of the two strong iron Kα lines are estimated to be 6.987 ± 0.005 keV and 6.714 ± 0.009 keV, suggesting a blue shift velocity of 900 ± 200 km s^{-1} and 700 ± 400 km s^{-1}, respectively. If we take only the first observation, the blue shifts become more significant with 1500^{+300}_{-200} km s^{-1} and 1500 ± 900 km s^{-1}, for the H-like and He-like irons, respectively. Here, the errors are statistical only. Given the current uncertainty in the gain calibration of ~ 20 eV or ~ 900 km s^{-1} (see § 2.3), the blue shift cannot be measured with higher significance. However, a blue shift is physically expected, since the material responsible for the absorption lines is certainly a wind from the disk (§ 1), and these values are consistent with the observed blue shift from other accreting systems like GRO J1655 − 40 (Miller et al. 2006) and GX 13 + 1 (Ueda et al. 2004). In the next subsection, the absorption line parameters and their time evolution are studied in detail.

3.3. Reanalysis of the absorption lines with Voigt profile

The simple gaussian analysis above shows significant He-like and H-like iron Kα absorption lines in the data, and suggests the presence of the weaker absorption structures at 7.8–8.2 keV. Since the parameters of the weaker high-energy lines are difficult to constrain, below we focus on the stronger two lines, and study them using 6.0–7.5 keV spectra. The limited energy range means that we do not need to include the (instrumental) broad gaussian at 10 keV or the narrow gaussian at 3.2 keV. We model

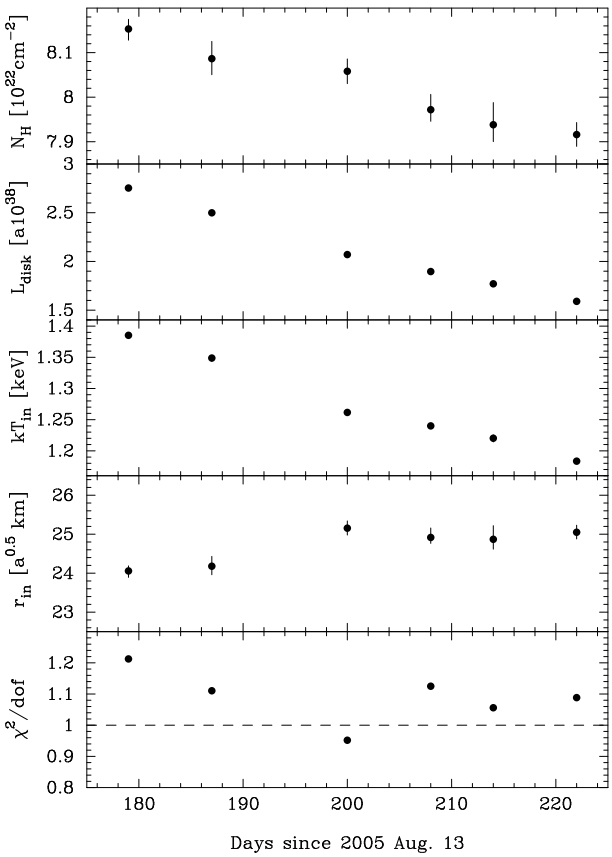

Fig. 4. Time histories of continuum parameters. Values of $N_{\rm H}$, $L_{\rm disk}$, $kT_{\rm in}$, $r_{\rm in}$, and χ^2/d.o.f are plotted. As described in the text, the decrease of $N_{\rm H}$ could be caused artificially by the over-simplified DISKBB model.

the continuum by DISKBB as before, with free parameters $T_{\rm in}$ and $r_{\rm in}$, but fix $N_{\rm H}$ to 8.0×10^{22} cm^{-2}, which is the average value obtained from the 2–10 keV fits. This does not affect the derived line center energies or equivalent widths, since the differences of $N_{\rm H}$ from the fixed value, at most $\sim 1 \times 10^{21}$ cm^{-2}, produce a rather small change to the iron edge at 7.1 keV.

To conduct a detailed analysis of these absorption lines, we use a full Voigt profile as implemented in the KABS model. The KABS model is constructed by Ueda et al. (2004) (see their §3.2.1) as a local model for XSPEC, and has three fitting parameters for each specific ion; the ion column density, $N_{\rm ion}$, the velocity dispersion, b, and the bulk outflow velocity characterized by a blue shift, z. The line shape is produced through a convolution of a Lorentzian profile, describing natural and pressure broadening with a gaussian describing Doppler motions (specified by the velocity dispersion including thermal and kinetic motion). Except for forbidden lines, each individual line of the Kα multiplet (Kα_1 and Kα_2) is included separately, with the appropriate energy, oscillator strength, and Einstein coefficient. This properly models the fine structure in the line even though these details of the line profile cannot be resolved by the CCD. The values of chi-squared are the same as for the previous negative gaus-

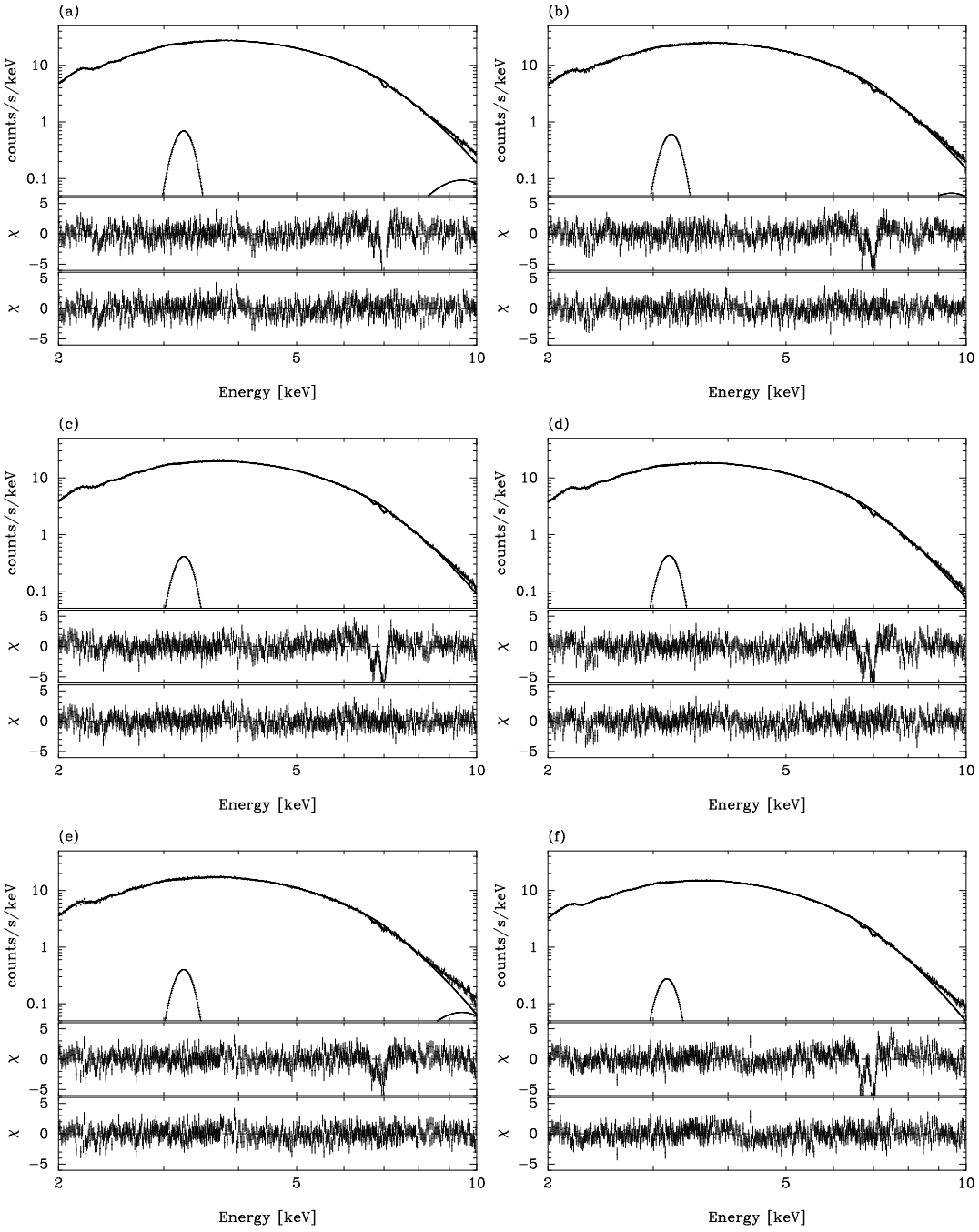

Fig. 3. XIS023 spectra for the first to the last observations in panel (a) to (f) in this order. The observed data and the best-fit DISKBB model with negative gaussians are shown in the top panels. The middle panels show residuals between the data and the model without negative gaussians. The bottom panels show the residuals between the data and the best-fit model. Note that the burst option was not used in the 5th and 6th observations (Table 1), hence the pileup effect is more obvious in panels (e) and (f) in spite of the gradual decrease of the source flux. An edge-like structure may be indicated at ~ 4 keV of which residual level is within 1%. This structure is understood as a coupling of calcium K edge at 4.05 keV of interstellar absorption and the uncertainty of current response matrix.

Table 2. Best-fit parameters for the 2–10 keV XIS spectra

epoch	continuum $N_{\rm H}$ [10^{22} cm^{-2}] $kT_{\rm in}$ [keV] $r_{\rm in}$ [$\sqrt{a}$ km]	gaussian 1 $E_{\rm c}$ [keV] EW [eV] (σ [eV]) *	gaussian 2 $E_{\rm c}$ [keV] EW [eV] (σ [eV]) *	gaussian 3 $E_{\rm c}$ [keV] EW [eV] significance under F-test †	gaussian 4 $E_{\rm c}$ [keV] EW [eV]	χ^2/dof
1	$8.15^{+0.02}_{-0.03}$ $1.385^{+0.004}_{-0.003}$ $24.1^{+0.1}_{-0.2}$	6.73 ± 0.02 7^{+1}_{-2} (< 37)	$7.001^{+0.006}_{-0.005}$ 30 ± 1 (< 49)	7.87 ± 0.04 $6.6^{+2}_{-3}(^{+0}_{-0.1})^{\ddagger}$ $F(566,4) = 5.69$	8.24 ± 0.05 $10.0^{+2}_{-4}(^{+0}_{-0.3})^{\ddagger}$ 99.98%	686.3/566
2	8.09 ± 0.04 $1.349^{+0.004}_{-0.005}$ $24.2^{+0.3}_{-0.2}$	$6.72^{+0.01}_{-0.02}$ 17 ± 3 (< 46)	$6.995^{+0.009}_{-0.008}$ 34^{+1}_{-4} (13^{+36}_{-13})	7.80 ± 0.05 $11.4 \pm 5(^{+0}_{-0.1})$ $F(566,4) = 9.68$	$8.24^{+0.03}_{-0.04}$ $23.1^{+2}_{-8}(^{+0}_{-0.5})$ $> 99.999\%$	628.6/566
3	8.06 ± 0.03 1.262 ± 0.003 $25.2^{+0.2}_{-0.2}$	6.72 ± 0.01 18 ± 2 (< 37)	$6.984^{+0.007}_{-0.006}$ 32 ± 2 (18 ± 18)	7.77 ± 0.08 $7.74 \pm 4(^{+0}_{-0.04})$ $F(566,4) = 6.89$	8.23 ± 0.04 $13.7^{+3}_{-5}(^{+0}_{-0.2})$ 99.998%	538.8/566
4	7.97 ± 0.03 $1.240^{+0.003}_{-0.004}$ $24.9^{+0.2}_{-0.2}$	6.72 ± 0.01 21 ± 3 (40^{+26}_{-21})	$6.980^{+0.009}_{-0.007}$ 30^{+2}_{-3} (< 66)	$7.84^{+0.04}_{-0.03}$ $18.2^{+4}_{-6}(^{+0}_{-0.1})$ $F(566,4) = 12.0$	$8.11^{+0.05}_{-0.06}$ $15.8^{+5}_{-7}(^{+0}_{-0.2})$ $> 99.999\%$	636.7/566
5	7.94 ± 0.04 $1.220^{+0.004}_{-0.005}$ $24.9^{+0.3}_{-0.3}$	6.72 ± 0.02 20 ± 4 (< 55)	6.97 ± 0.01 28^{+3}_{-5} (40^{+25}_{-40})	(7.8–7.9)§ < 13 $F(566,4) = 0.34$	(8.2–8.3)§ < 10 15%	599.9/566
6	7.92 ± 0.03 1.183 ± 0.003 $25.1^{+0.2}_{-0.2}$	6.705 ± 0.009 22^{+2}_{-3} (22^{+25}_{-22})	$6.969^{+0.008}_{-0.006}$ 31 ± 2 (< 23)	7.85 ± 0.09 6^{+4}_{-5} $F(566,4) = 1.05$	(8.2–8.3)§ < 9 62%	616.0/566

Notes. Errors represents 90% confidence limit of the statistical errors. See §2.3 for systematic errors.

* The best-fit values of σ, or the upper limit if the best-fit value is smaller than 10 eV.

† F-values are presented for the addition of gaussians 3 and 4.

‡The best fit normalization factors of the broad gaussian at 10 keV for the pileup are 7.0, 4.1, 2.4, 1.9, 5.2, and 3.1×10^{-3} photons s^{-1} cm^{-2}, in order of the first to the last observations. Uncertainty of the pileup effect to the equivalent width is considered by including/excluding the broad gaussian to the corresponding continuum.

§ Line center energies are fixed at those of He-like and H-like iron Kβ in the rest frame to obtain upper limits of the equivalent width, since they are not constrained by the fitting.

sian fits, but this model gives the ion column $N_{\rm ion}$ for an assumed velocity dispersion, b, as opposed to simply an equivalent width. We require the two lines to have the same b and the same z, and neglect any line emission which could fill in the absorption.

Although we cannot measure b from line profiles, its upper and lower bounds may be obtained. The upper limit is set at $b \sim 2000$ km s^{-1} by the upper limits on the line width, $\sigma \sim 30$–40 eV (§ 3.2). The lower limit to b is given by the thermal velocity. At such high ionization, the self-consistent temperature of the photoionized material must be of order the Compton temperature, $T_{\rm C}$. Considering the balance between Compton heating by the dominant disk illumination, and Compton, bremsstrahlung and ion coolings, $T_{\rm C}$ is roughly estimated as $kT_{\rm in}/3$ (i.e., 0.5 keV in this case). The flux in the power-law tail has only a very small effect on this as it is so much weaker than the disk (20–100 keV power-law flux is only $\sim 1\%$ of the disk bolometric flux), and does not contribute significantly on the compton heating (e.g., Reynolds & Wilms 2000). This temperature implies thermal (random kinetic) velocties as $b = \sqrt{2kT_{\rm C}/m_{\rm atom}}$, and thus $b = 42$ km s^{-1} can be obtained as a secure lower limit.

Table 3 gives the derived $N_{\rm ion}$ for these two limiting velocities, together with velocities of $b = 100$, 200, and 500 km s^{-1}. As expected from the curve-of-growth analysis, the observed equivalent width can be produced by a lower value of $N_{\rm ion}$ if a higher value of b is assumed. In Table 3, we can put further constraints on b by using the observed equivalent widths of weaker lines at 7.8 keV and 8.2 keV (gaussian 3 and 4 in Table2). The table includes the model predictions for the equivalent width of the iron Kβ absorption lines. There, models with "1" in the last column ("Note") are inconsistent, because the predicted iron Kβ line equivalent widths exceeds the actually observed values, leaving no room for the nickel Kα lines to contribute. By scanning b with finer steps, we found that b of $\sim$ 60–200 km s^{-1} significantly over predicts the Kβ equivalent width, and is hence ruled out.

The top three panels of figure 7 show the time histories of the best-fit KABS parameters, assuming $b = 500$ km s^{-1} which is based on the marginally resolved line width in the Chandra HETGS data of GX $13+1$ (Ueda et al. 2004). The column density of the H-like iron, $N_{\rm Fe\ XXVI}$, is almost constant at $\sim 1 \times 10^{18}$ cm^{-2} while that of the He-like iron, $N_{\rm Fe\ XXV}$, increases significantly from the first to the second observation. This is consistent with the behavior of the equivalent width estimated using the negative gaus-

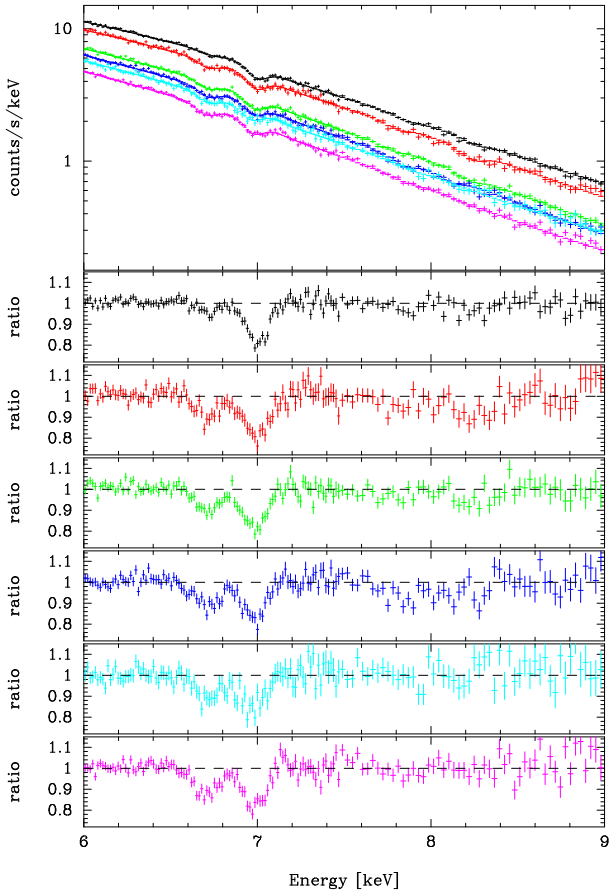

Fig. 5. The XIS023 6-9 keV spectra concentrating on the absorption line structure. Data and the best-fit models (Table 2) are shown in the top panel. Residuals between the data and the best-fit model excluding the four negative gaussians are shown in the successive six panels. Colors are the same as in figure 2.

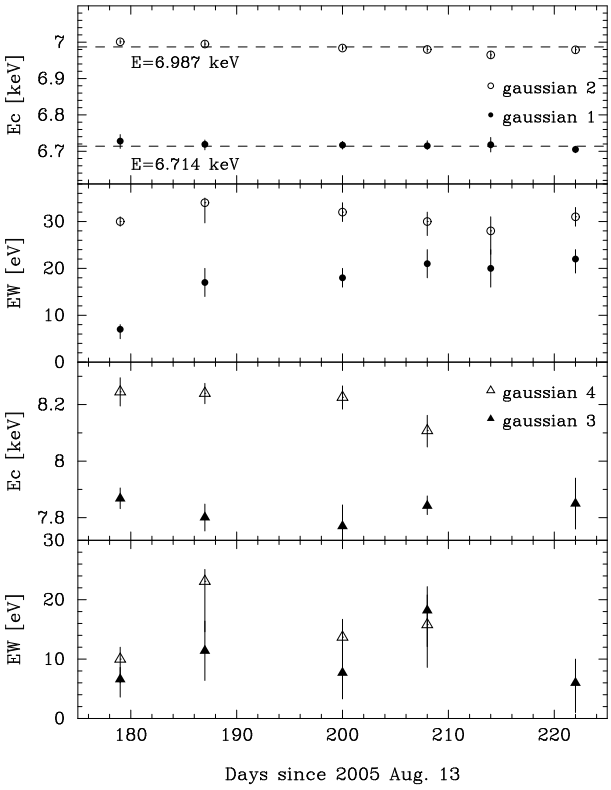

Fig. 6. Time histories of absorption line parameters based on the negative gaussian fit in the range of 6–10 keV. The first two panels show line center energies and equivalent width of gaussian 1 (filled circle) and gaussian 2 (open circle). The bottom two panels show those of gaussian 3 (filled triangle) and gaussian 4 (open triangle). On the top panel, average values are shown with dashed lines.

sian fit (Table 2). The weighted average blue shift is about $z = (3.3 \pm 0.7) \times 10^{-3}$, corresponding to an outflow velocity of 1000 ± 200 km s^{-1}. Again, the first observation shows $z = (5.0^{+0.8}_{-0.6}) \times 10^{-3}$ or $v = 1500^{+240}_{-180}$ km s^{-1} (see Table 3). They are consistent with the results obtained with the negative gaussian fits in § 3.2.

4. Physical parameters of the absorber

We observed very significant absorption lines from He–like and H–like iron Kα in the disk dominated X-ray spectrum of 4U 1630 − 472 during its decline from outburst. The inferred blue shift of the absorption lines supports the presence of an outflow. This source thus joins the growing number of Galactic binaries with such absorption features, suggesting that winds are a generic feature of bright accretion disks observed at high inclination angles. Through the analyses in § 3, we found that iron is always predominantly H–like, requiring that the ionization parameter, $\xi = L/nr^2$ (where n and r are the number density and the distance of the absorbing material from the illuminating source), be very high. In this section, we use the XSTAR photoionization code[3] (version 2.1kn5, Kallman & Bautista 2001) to calculate the ionization balance of the line-producing material, to convert the ion column densities into physical parameters including total column density, number density, and location, for each observation.

4.1. *First observation*

We derive the physical parameters of the absorber using the first observation as a specific example to illustrate the method. We calculate the relative ion populations under illumination by a DISKBB spectrum, and use this to predict a theoretical ratio of $N_{\rm Fe\ XXV}$ to $N_{\rm Fe\ XXVI}$. The observed ratio from the data then enables us to estimate the ξ-parameter, and so convert the observed ion column densities of H-like and He-like irons into a total column density, $N_{\rm tot}$.

We use the illuminating spectrum derived from the Suzaku data, i.e., a DISKBB spectrum of $kT_{\rm in} = 1.4$ keV, to calculate the self-consistent ion populations of iron using XSTAR. The solid lines in figure 8a shows the calculated relative fractions of each ionization stage of iron, $f_{\rm ion}$, against ξ, while figure 8b shows $N_{\rm Fe\ XXV}/N_{\rm Fe\ XXVI}$.

[3] http://heasarc.gsfc.nasa.gov/docs/software/xstar/xstar.html

Table 3. Best-fit parameters of the 6–7.5 keV KABS model

epoch	The best-fit KABS parameters				predicted Kβ EW*		$N_{\rm ion}$ ratio†	plasma parameters‡		Note§
	$N_{\rm Fe\ XXV}$	$N_{\rm Fe\ XXVI}$	$z^{\parallel}$	χ^2	Fe XXV	Fe XXVI	He/H	ξ	$N_{\rm tot}$	
	10^{18} cm^{-2}	10^{18} cm^{-2}	10^{-3}	(96)#	eV	eV	$\times10^{-2}$	10^4	10^{23} cm^{-2}	
$b=42$ km s^{-1} ($kT_{\rm kin}=0.5$ keV)										
1	$0.6^{+0.4}_{-0.3}$	34^{+6}_{-5}	$5.2^{+0.7}_{-0.7}$	116.1	4.1	12.5	$1.7^{+1.6}_{-1.0}$	19^{+15}_{-7}	130^{+140}_{-60}	2
2	$4.9^{+2.2}_{-2.0}$	40^{+10}_{-9}	$4.2^{+1.0}_{-1.1}$	97.9	9.3	11.3	12^{+10}_{-6}	5^{+4}_{-2}	39^{+39}_{-16}	2
3	$4.4^{+1.6}_{-1.2}$	33^{+7}_{-6}	$2.8^{+1.0}_{-0.8}$	98.8	7.9	12.6	14^{+9}_{-5}	6^{+3}_{-2}	29^{+18}_{-10}	2
4	$6.7^{+2.3}_{-2.0}$	31^{+7}_{-6}	$2.4^{+1.3}_{-0.7}$	102.4	10.1	11.8	22^{+15}_{-9}	5^{+2}_{-1}	22^{+12}_{-6}	2
5	$5.7^{+3.5}_{-2.3}$	27^{+11}_{-8}	1.5 ± 1.5	85.7	8.1	10.3	21^{+28}_{-12}	5^{+5}_{-2}	$1.9^{+2.1}_{-0.7}$	2
6	$7.7^{+2.5}_{-1.8}$	33^{+4}_{-6}	$1.9^{+1.0}_{-0.8}$	108.2	10.3	12.0	24^{+15}_{-7}	6 ± 2	22^{+6}_{-5}	1,2
$b=100$ km s^{-1} ($kT_{\rm kin}=2.9$ keV)										
1	$0.23^{+0.14}_{-0.09}$	24^{+6}_{-4}	$5.3^{+0.7}_{-0.7}$	115.9	3.1	17.1	$1.0^{+1.0}_{-0.5}$	29^{+19}_{-11}	140^{+130}_{-70}	1, 2
2	$2.03^{+1.30}_{-0.80}$	31^{+10}_{-9}	$4.4^{+1.0}_{-1.1}$	98.0	11.3	17.6	7^{+9}_{-4}	8^{+6}_{-4}	45^{+58}_{-25}	2
3	$1.98^{+0.97}_{-0.78}$	23^{+7}_{-6}	$3.0^{+0.9}_{-0.8}$	99.2	11.1	17.1	9^{+9}_{-5}	9^{+6}_{-3}	26^{+30}_{-12}	2
4	$3.12^{+1.46}_{-1.07}$	21^{+7}_{-6}	$2.7^{+1.2}_{-0.8}$	103.5	12.9	16.8	15^{+16}_{-8}	6^{+4}_{-3}	17^{+17}_{-8}	2
5	$2.51^{+2.17}_{-1.17}$	17^{+10}_{-8}	$1.8^{+1.6}_{-1.6}$	87.5	11.9	16.4	15^{+37}_{-10}	7^{+8}_{-4}	14^{+27}_{-8}	1, 2
6	$3.99^{+1.62}_{-1.21}$	22^{+7}_{-6}	$2.3^{+0.8}_{-0.9}$	107.2	13.9	17.0	18^{+16}_{-8}	7^{+4}_{-2}	16^{+12}_{-6}	1, 2
$b=200$ km s^{-1} ($kT_{\rm kin}=12$ keV)										
1	$0.14^{+0.05}_{-0.04}$	$3.6^{+1.2}_{-0.9}$	$5.4^{+0.7}_{-0.7}$	115.6	2.2	15.6	4^{+3}_{-2}	11^{+6}_{-4}	8^{+8}_{-4}	1
2	$0.66^{+0.34}_{-0.22}$	$5.0^{+3.2}_{-1.8}$	$4.3^{+1.0}_{-1.1}$	99.8	8.1	17.8	13^{+18}_{-8}	5^{+4}_{-2}	5^{+9}_{-3}	
3	$0.65^{+0.13}_{-0.18}$	$3.4^{+1.6}_{-1.0}$	$3.0^{+0.9}_{-0.8}$	98.9	8.0	15.2	19^{+13}_{-10}	5^{+3}_{-2}	3^{+3}_{-1}	
4	$0.92^{+0.35}_{-0.26}$	$3.0^{+1.4}_{-0.9}$	$2.6^{+1.2}_{-0.7}$	103.8	9.9	14.3	30^{+29}_{-15}	4^{+3}_{-1}	$2.0^{+1.7}_{-0.7}$	
5	$0.77^{+0.49}_{-0.31}$	$2.3^{+1.9}_{-0.9}$	$1.5^{+1.7}_{-1.5}$	87.2	9.1	12.3	33^{+56}_{-22}	4^{+5}_{-2}	$1.5^{+2.5}_{-0.6}$	1
6	$1.16^{+0.40}_{-0.30}$	$3.4^{+1.5}_{-1.0}$	$2.3^{+0.8}_{-0.8}$	107.4	11.6	15.0	35^{+30}_{-17}	4^{+3}_{-2}	$2.2^{+1.5}_{-0.6}$	1
$b=500$ km s^{-1} ($kT_{\rm kin}=72$ keV)										
1	$0.11^{+0.03}_{-0.03}$	$1.14^{+0.13}_{-0.12}$	$5.0^{+0.8}_{-0.6}$	115.6	1.9	8.5	10^{+4}_{-3}	$5.6^{+1.9}_{-1.2}$	$1.3^{+0.6}_{-0.3}$	
2	$0.29^{+0.08}_{-0.06}$	$1.27^{+0.24}_{-0.20}$	$4.0^{+1.0}_{-1.1}$	99.8	4.7	9.7	23^{+12}_{-8}	$3.3^{+1.1}_{-0.9}$	$0.9^{+0.4}_{-0.2}$	
3	$0.30^{+0.06}_{-0.03}$	$1.11^{+0.17}_{-0.15}$	$2.6^{+1.1}_{-0.8}$	98.7	4.9	8.3	27^{+10}_{-6}	$3.8^{+0.8}_{-0.7}$	0.8 ± 0.2	
4	$0.36^{+0.08}_{-0.06}$	$1.05^{+0.18}_{-0.15}$	$2.2^{+1.3}_{-0.7}$	103.7	5.4	8.0	34^{+14}_{-10}	$3.5^{+1.0}_{-0.8}$	$0.7^{+0.2}_{-0.1}$	
5	$0.34^{+0.10}_{-0.09}$	$0.95^{+0.23}_{-0.20}$	$1.1^{+1.6}_{-1.5}$	86.3	5.4	7.7	35^{+23}_{-15}	$3.6^{+1.6}_{-1.1}$	$0.6^{+0.2}_{-0.1}$	
6	$0.41^{+0.08}_{-0.07}$	$1.10^{+0.18}_{-0.15}$	$1.6^{+1.0}_{-0.3}$	108.3	6.5	8.5	37^{+14}_{-10}	$4.0^{+1.1}_{-0.8}$	$0.7^{+0.2}_{-0.1}$	
$b=2000$ km s^{-1}($kT_{\rm kin}=1200$ keV)										
1	$0.11^{+0.01}_{-0.03}$	$0.89^{+0.06}_{-0.06}$	$5.0^{+0.7}_{-0.6}$	123.7	1.9	7.2	12^{+2}_{-4}	$4.7^{+1.4}_{-0.5}$	$0.89^{+0.3}_{-0.1}$	
2	$0.26^{+0.05}_{-0.04}$	$0.97^{+0.13}_{-0.10}$	$4.0^{+1.1}_{-1.1}$	95.0	4.1	8.5	27^{+9}_{-7}	$3.0^{+0.7}_{-0.5}$	$0.7^{+0.2}_{-0.1}$	
3	$0.26^{+0.04}_{-0.04}$	$0.87^{+0.09}_{-0.09}$	$2.5^{+1.0}_{-0.8}$	101.1	4.5	7.1	30^{+8}_{-7}	$3.6^{+0.7}_{-0.6}$	0.6 ± 0.1	
4	$0.29^{+0.05}_{-0.04}$	$0.84^{+0.06}_{-0.08}$	$2.2^{+1.1}_{-0.9}$	100.2	4.9	7.5	35^{+10}_{-6}	$3.5^{+0.6}_{-0.6}$	0.53 ± 0.06	
5	$0.28^{+0.07}_{-0.05}$	$0.80^{+0.13}_{-0.14}$	$1.1^{+0.9}_{-1.6}$	82.6	4.4	6.9	35^{+18}_{-11}	$3.7^{+1.0}_{-0.9}$	0.5 ± 0.1	
6	$0.32^{+0.04}_{-0.03}$	$0.87^{+0.08}_{-0.08}$	$1.6^{+1.1}_{-0.8}$	110.4	5.1	6.9	37^{+9}_{-7}	$4.0^{+0.6}_{-0.6}$	0.55 ± 0.06	

Notes. Errors represents 90% confidence limit of statistical errors. See § 2.3 for systematic errors. * Predicted equivalent width of He-like and H-like iron Kβ under the best-fit KABS model. † Ratio of $N_{\rm Fe\ XXV}$ to $N_{\rm Fe\ XXVI}$ from the best-fit values. ‡ ξ-parameters and total column density are calculated based on equations (1) and (2) derived in §4. § The models are rejected based on overestimation of Kβ equivalent width (denoted as 1) or large $N_{\rm tot}$ as $>1.6\times10^{24}$ cm^{-2} (denoted as 2). $^{\parallel}$ Plus is defined as blue shift. # Degrees of freedom.

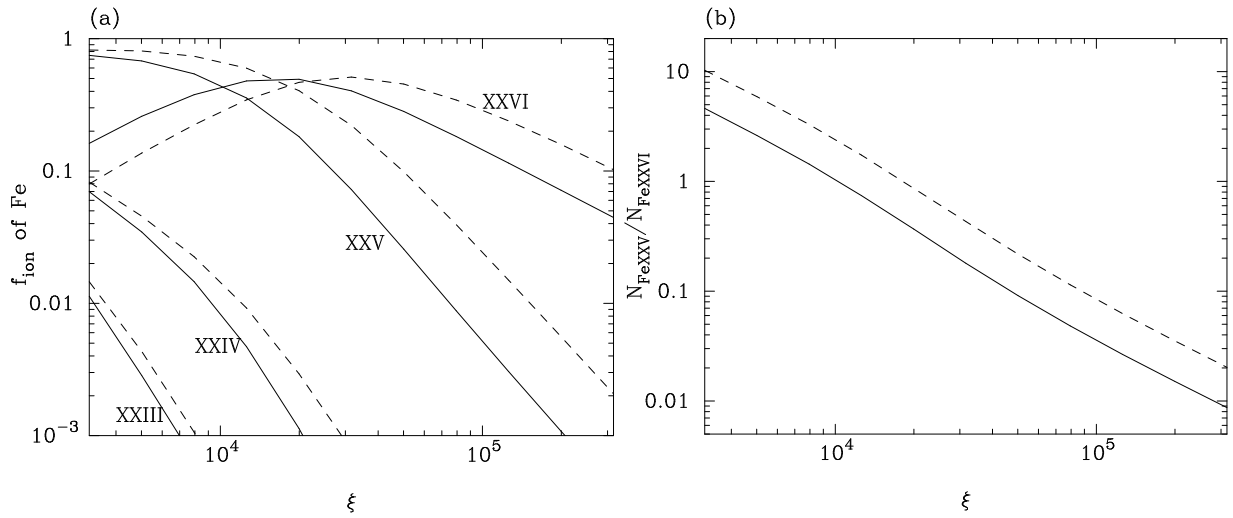

Fig. 8. Relative ionization population, $f_{\rm ion}$, of iron (a) and the ratio of He-like to H-like iron (b), shown as a function of the ionization parameter ξ. Photoionization-recombination equilibrium is assumed in an X-ray irradiated matter with a small optical depth. The irradiating X-ray spectral shape is assumed to be a DISKBB of $kT_{\rm in} = 1.4$ keV (solid line) and $kT_{\rm in} = 1.2$ keV (dashed line).

The ratio can be well approximated by a power law, as $N_{\rm Fe\ XXV}/N_{\rm Fe\ XXVI} \approx 4 \times 10^5 \cdot \xi^{-1.4}$. Similarly, we obtain the fraction of H-like iron as $f_{\rm XXVI} \approx 1.2 \times 10^4 \cdot \xi^{-0.98}$ at high values of ξ (roughly $\xi > 3 \times 10^4$). Since a value of $N_{\rm tot}$ is obtained as $N_{\rm tot} \cdot A_{\rm Fe} \cdot f_{\rm XXVI} = N_{\rm Fe\ XXVI}$, where $A_{\rm Fe} = 3.3 \times 10^{-5}$ is the solar iron abundance, it can be estimated as $N_{\rm tot} = N_{\rm Fe\ XXVI}/(A_{\rm Fe} \cdot f_{\rm XXVI})$. By using these relations, we derive ξ and $N_{\rm tot}$ for the range of b given in Table 3. The derived values of ξ, $N_{\rm tot}$ and $N_{\rm XXV}/N_{\rm XXVI}$ are also summarized in the same table. In general, all these quantities are anti-correlated with b, and at low velocity dispersions of $b = 42$ and 100 km s^{-1}, $N_{\rm tot}$ exceeds 1.6×10^{24} cm^{-2} i.e., is optically thick to electron scattering. This case is indicated as "2" in the last column ("Note") of the table. Thus, the case of $b \leq 100$ km s^{-1} is ruled out by both the Kβ absorption structures and the condition of optically thin scattering. We can thus conclude that there must be higher velocities present than expected simply from the temperature of the material, pointing to the importance of either a structured velocity field as expected in an accelerating outflow, and/or turbulence.

4.2. Time evolution of the absorber

We repeat the above analysis for all the datasets. Since the value of $kT_{\rm in}$ changes as the source decline, we calculate XSTAR models $T_{\rm in}$ spanning the observed range of 1.2, 1.3, and 1.4 keV, and then use this to interpolate the ion populations for each observed temperature. The dashed lines in figure 8 show the results with $kT_{\rm in} = 1.2$ keV, in comparison with the solid lines which assumes $kT_{\rm in} = 1.4$ keV. We approximated the behavior of the ratio of He-like to H-like ion columns and $f_{\rm XXVI}$ by following two formulae,

$$N_{\rm Fe\ XXV}/N_{\rm Fe\ XXVI} = 4 \times 10^5 \cdot (kT_{\rm in}/1.4)^{-5.57} \cdot \xi^{-1.4} \quad , (1)$$

$$\log(f_{\rm XXVI}) = -2 + 1.69 \cdot \exp\left(\frac{-(\log(\xi/\xi_0))^2}{2}\right) \quad , \quad (2)$$

where $f_{\rm XXVI}$ peaks at $\log(\xi_0) = 4.13 \cdot (kT_{\rm in}/1.4)^{-0.53}$. Using these formulae, we converted the observed values of $N_{\rm XXV}/N_{\rm XXVI}$ and $N_{\rm XXVI}$ into $N_{\rm tot}$ and ξ, as given in Table 3. For all the data sets, $b = 42$ km s^{-1} ($kT_{\rm kin} = 0.5$ keV) and $b = 100$ km s^{-1} are again ruled out because $N_{\rm tot}$ becomes optically thick, as well as generally over-predicting the iron Kβ absorption (§ 3.3).

The inferred time histories of the values of ξ and $N_{\rm tot}$ are shown in figure 7 assuming $b = 500$ km s^{-1}, together with upper and lower bounds corresponding to $b = 200$ and 2000 km s^{-1}. Assuming that the velocity dispersion stays constant at $b = 500$ km s^{-1} then there is a marginal decrease in $N_{\rm tot}$ as the luminosity decreases, from $\sim 1 \times 10^{23}$ cm^{-2} in the first observation to $\sim 7 \times 10^{22}$ cm^{-2} in the final dataset, as well as a marginal decrease in ξ from $\sim 6 \times 10^4$ to $\sim 4 \times 10^4$.

4.3. Location of absorbers

We can roughly estimate n and r of the absorbing plasma, by using the definitions of $N_{\rm tot} = \int_{R_0}^{\infty} n \cdot dr$ and $\xi = L/nr^2$ where R_0 is the launching radius of the absorber. In this section, we use $b = 500$ km s^{-1} to estimate ξ and $N_{\rm tot}$, and choose to replace luminosity with flux, so as to make the dependence on the poorly constrained source distance explicit. We parameterize this in terms of D_{10}, denoting distance in units of 10 kpc, and note there is no uncertainty in ξ parameter associated with the inclination, since the absorber is along the same line of sight as we are.

The description of $N_{\rm tot}$ can be simplified as $N_{\rm tot} = \bar{n}\Delta R$ with a mean number density $\bar{n}$ and a characteristic thickness of the absorber ΔR. Using $\xi = L/\bar{n}R^2$, the average distance of the absorber, R, is thus estimated as $R \sim 3 \times 10^{10} \cdot (\Delta R/R) \cdot {D_{10}}^2$ and $\sim 4 \times 10^{10} \cdot (\Delta R/R) \cdot {D_{10}}^2$ cm, for

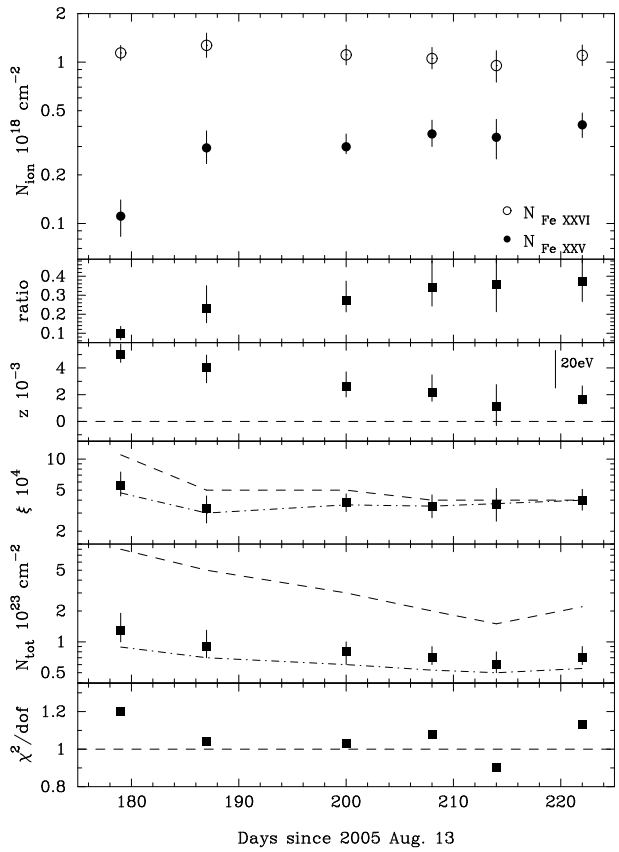

Fig. 7. Time histories of absorption line parameters based on the Voigt profile fitting for $b = 500$ km s^{-1}. The top panel shows column density of H-like (open circle) and He-like iron (filled circle) in unit of 10^{18} cm^{-2}, the second panel shows $N_{\rm Fe\ XXV}/N_{\rm Fe\ XXVI}$, and the third panel shows the line blue shift, z, in unit of 10^{-3}. Systematic uncertainty of ~ 20 eV for the absolute energy is interpreted as the uncertainty of z as $\Delta z \sim 3 \times 10^{-3}$ at 7 keV, which is also shown in the third panel. Based on the ratio, ξ-parameter and the total hydrogen column $N_{\rm tot}$ are calculated and are shown in the next two panels in units of 10^4 and 10^{23} cm^{-2}, respectively. The best estimation of ξ and $N_{\rm tot}$ for $b = 200$ km s^{-1}(dashed line) and 2000 km s^{-1} (dash-dot line) are also shown in the same panels.

the first and the last observations, respectively. The densities are also estimated as $\bar{n} \sim 5 \times 10^{12} \cdot (\Delta R/R)^{-2} \cdot {D_{10}}^{-2}$ and $\sim 2 \times 10^{12} \cdot (\Delta R/R)^{-2} \cdot {D_{10}}^{-2}$ atoms cm^{-3}. Assuming $\Delta R/R \sim 1$ by following the previous research (e.g., Kotani et al. 2000; Ueda et al. 2001; 2004), the values of R and $\bar{n}$ are estimated to be on the order of $R \sim 10^{10} \cdot {D_{10}}^2$ cm and $\bar{n} \sim 10^{12} \cdot {D_{10}}^{-2}$ atoms cm^{-3}. They depend on the plasma thickness $\Delta R/R$, and the longer distance and higher density are realized on the the condition of smaller $\Delta R/R$. However, since this structure is continuous, it seems unlikely to have too small thickness (e.g., $\Delta R/R < 0.1$). Thus the range of the distance can be securely estimated as $10^{9-10} \cdot {D_{10}}^2$ cm. This value is well consistent with those estimated from the other binaries which showed absorption line structures.

Because of lack of any evidence for low ionization material, it is reasonable and convenient to assume a constant ionization state throughout the matter. We thus assume that n drops as r^{-2} to keep ξ constant at different distances. This is also physically realistic for a geometrically thick absorber, since mass conservation requires this dependency for a constant outflow velocity with constant opening angle. In this case, $N_{\rm tot}$ and ξ are described as $N_{\rm tot} = n_0 R_0$ and $\xi = L/n_0 {R_0}^2$, respectively, where n_0 is the launching density at R_0. The launching distance is thus estimated as $R_0 \sim (3\text{–}4) \times 10^{10} \cdot {D_{10}}^2$ cm throughout the observations, with the associated density of $n_0 \sim (5\text{–}2) \times 10^{12} \cdot D_{10}^{-2}$ cm^{-3}. These values are in good agreement with the previous estimation of the mean distance R as expected as averaging the density profile gives an effective width of $\Delta R/R_0 \sim 0.7$. There are no significant changes over the six observations, but the data are consistent with a small increase in R_0 and/or a small decrease in n_0 as the luminosity decreases. There are some uncertainties on these numbers due to the statistical uncertainties in $N_{\rm tot}$ and ξ, but the larger source of uncertainty is systematic from the assumed velocity dispersion of $b = 500$ km s^{-1}. The lower limit on b gives an upper limit on $N_{\rm tot}$ and ξ, and thus results in smaller launching radius with larger density. Considering our range in b of 200–2000 km s^{-1}, the allowed range of R_0 is estimated to be $(0.2\text{–}4) \times 10^{10} \cdot {D_{10}}^2$ cm and $(1\text{–}5) \times 10^{10} \cdot {D_{10}}^2$ cm for the first and the last observations, respectively.

5. The nature of the wind

The estimated launch radii are much smaller than the distance traveled by the absorbing material over a single 20 ks observation from the measured blue shift of ~ 1000 km s^{-1}, $10^{12} \cdot D_{10}^2$ cm. Thus the persistence of the wind over the two-month monitoring period, where the source was always in the high/soft state, shows that the material is not associated with a one–off event such as a state transition. Neither can it be connected to the jet since the radio emission is strongly suppressed in the high/soft state (Fender et al. 1999). Instead it must be produced by the disk in a continuous or quasi-continuous manner.

Here we use the estimated physical parameters of the absorber to constrain the driving mechanism for this wind. One of the candidate mechanisms is radiation pressure on electrons, which becomes dynamically important as L approaches $L_{\rm Edd}$, reducing the effective gravity by a factor $\sim (1 - L/L_{\rm Edd})$. This can be made much more efficient if the cross-section for interaction between the matter and radiation is enhanced by line opacity. There are multiple line transitions in the UV region of the spectrum, so UV emitting disks can drive a powerful wind at luminosities far below Eddington. Such line driven disk winds are seen in CV's (Pereyra et al. 2000) and are probably also responsible for the broad absorption line (BAL) outflows seen in AGN (Proga, Stone, Kallman 2000). However, the disk temperature for black hole binaries is in the X-ray regime, so line driving is probably unimportant here (Proga & Kallman 2002). We do indeed see lines, but the momentum absorbed in these iron transitions is very

small, completely insufficient to drive the wind.

Another type of outflow from a disk is a thermally driven wind (Begelman et al. 1983). Here again the central illumination is important, but the process is less direct. The illumination heats the upper layers of the disk to a temperature of order the Compton temperature, $T_{\rm C}$. This will expand due to the pressure gradient, and at large enough radii the thermal energy driving the expansion is larger than the binding energy, leading to a wind from the outer disk. Simple estimates of the launching radius of this wind give $R = 10^{10} \cdot (M/M_{\odot}) \cdot (T_{\rm C}/10^8\ {\rm K})^{-1} \sim 10^{12}$ cm (Begelman et al. 1983). This is a much larger distance than inferred for our wind. However, this is an overestimate, and a more careful analysis shows that thermal winds are launched at a radius a factor 5–10 smaller than this (Begelman et al. 1983; Woods et al. 1996) . Secondly, the *combination* of thermal driving and radiation pressure from moderately sub-Eddington illumination can be much more effective at producing a wind. The hydrodynamic calculation of Proga & Kallman (2002) shows that thermal driving with $L/L_{\rm Edd} = 0.6$ gives a powerful wind from well within the expected thermal driving radius. Their simulation is not exactly matched to the situation here, as they model a neutron star rather than a black hole. Nonetheless, their wind is launched from a distance of around $1000R_{\rm s}$, has a column between 10^{22-23} cm^{-2} and ionization of $\xi \sim 10^5$ for inclinations larger than 70°. This is very close to our inferred parameters for the wind seen here in 4U 1630−472. The simulation even has an outflow velocity of ~ 1000 km s^{-1} as currently indicated by the data.

The last type of outflow is a magnetically driven wind. These are much harder to quantitatively study as the magnetic field configuration is not known, yet they are almost certainly present at some level as the underlying angular momentum transport is known to be due to magnetic fields (see e.g. Balbus & Hawley 2002). Winds (and jets) are clearly present in magnetohydrodynamical (MHD) simulations which include these magnetic stresses self consistently. These generically show that the mass loss is stochastic, with large fluctuations both spatially and temporally, but that the time averaged properties are well defined, so this magnetic wind is quasi-continuous (e.g., Hawley & Krolik 2001; Machida, Nakamura, & Matsumoto 2004). These calculations are still in their infancy, especially for describing the properties of a geometrically thin disk as appropriate here, so cannot yet be used for quantatiative predictions of the wind in the high/soft state. Instead, an approximation to the properties of the self-consistent magnetic wind from an accretion disk can be made by imposing an external field geometry (Proga 2000; 2003). The mass loss rates depend on this field configuration, but in general these allow steady, powerful winds to be launched from any radius. This lack of diagnostic power means that they can be reliably identified only when all other potential mechanisms for a wind are ruled out.

While the physical parameters required for the absorbing material seen in 4U 1630 − 472 are somewhat more extreme than produced by the simple analytic estimates of a thermally driven wind, they seem to be potentially within the range of composite thermal/radiation pressure driven winds if $L/L_{\rm Edd} > 0.1$. Unfortunately there are no firm estimates for the distance and black hole mass for 4U 1630 − 472, and thus the Eddington ratio ($L/L_{\rm Edd} \sim 0.2$–$0.3 \cdot a$) is hard to constrain. Neither are there any directly applicable simulations of these winds, and how their properties might change with $L/L_{\rm Edd}$ decreasing by a factor 1.7. Hence there is no unambiguous requirement for magnetic driving from these data. Nonetheless, this wind is clearly very similar in properties (though with a slightly higher ionization state) to that that seen in a similar high/soft state from another black hole, GRO J1655-40, where Miller et al. (2006) inferred a very small launching radius from the Chandra grating data requiring a magnetic wind. Given the continuity of properties seen between the wind in 4U 1630 − 472 and GRO J1655 − 40 then it seems likely that if the wind in GRO J1655 − 40 is magnetically driven, then this process is important also in the 4U 1630 − 472 absorber examined here.

We are grateful to all the Suzaku team members. We also thank Tim Kallman for making the XSTAR package publicly available. A.K. is supported by a special postdoctoral researchers program in RIKEN. T.K. is supported by the Japan-Russia Research Cooperative Program of JSPS. C.D. thanks ISAS for hospitality during the period over which this work was carried out. The present work is supported in part by Grant-in-Aid No.1703011 from Ministry of Education, Culture, Sports, Science and Technology of Japan.

References

Abe, Y., Fukazawa, Y., Kubota, A., Kasama, D., & Makishima, K. 2005, PASJ, 57, 629
Augusteijn, T., Kuulkers, E., & van Kerkwijk, M. H. 2001, A&A, 375, 447
Balbus, S. A., & Hawley, J. F. 2002, ApJ, 573, 749
Begelman, M. C., McKee, C. F., & Shields, G. A. 1983, ApJ, 271, 70
Bloser, P. F., Barret, D., Grindlay, J. E., Zhang, S. N., Harmon, B. A., Fishman, G. J., & Paciesas, W. S. 1996, A&AS, 120, 191
Boirin, L., & Parmar, A. N. 2003, A&A, 407, 1079
Boirin, L., Parmar, A. N., Barret, D., Paltani, S., & Grindlay, J. E. 2004, A&A, 418, 1061
Blandford, R. D., & Payne, D. G. 1982, MNRAS, 199, 883
Cui, Q., Chen, W., & Zhang, S. N. 2000, ApJ, 529, 952
Church, M. J., Reed, D., Dotani, T., Bałucińska-Church, M., & Smale, A. P. 2005, MNRAS, 359, 1336
Davis, S. W., Blaes, O. M., Hubeny, I., & Turner, N. J. 2005, ApJ, 621, 372
Dieters, S. W., et al. 2000, ApJ, 538, 3307
Drake, G. W. 1988, Canadian J. Phys., 66, 586
Fender, R., et al. 1999, ApJL, 519, L165
Hawley J. F., Krolik J. H., 2001, ApJ, 548, 348
Hjellming, R. M., et al. 1999, ApJ, 514, 383

Jones, C., Forman, W., Tananbaum, H., & Turner, M. J. L. 1976, ApJ, 210, L9
Kalemci, E., Tomsick, J. A., Rothschild, R. E., Pottschmidt, K., & Kaaret, P. 2004, ApJ, 603, 231
Kallman T. R., Angelini L., Boroson B., Cottam J., 2003, ApJ, 583, 861
Kallman, T., & Bautista, M. 2001, ApJS, 133, 221
Kuulkers, E., van der Klis, M., & Parmar, A. N. 1997, ApJL, 474, L47
Kuulkers, E., Wijnands, R., Belloni, T., Mendez, M., van der Klis, M., & van Paradijs, J. 1998, ApJ, 494,753
Kokubun, M., et al. 2006, PASJ, submitted
Kotani, T., Ebisawa, K., Dotani, T., Inoue, H., Nagase, F., Tanaka, Y., & Ueda, Y. 2000, ApJ, 539, 413 Erratum: —, 2006, ApJ, in press, astro-ph/0003237
Koyama, K. et al. 2006, PASJ, accepted
Kubota, A., & Makishima, K., 2004, ApJ, 601, 428
Lee, J. C., Reynolds, C. S., Remillard, R., Schulz, N. S., Blackman, E. G., & Fabian, A. C. 2002, ApJ, 567, 1102
Levine, A. M., Bradt, H., Cui, W., Jernigan, J. G., Morgan, E. H., Remillard, R., Shirey, R. E., & Smith, D. A. 1996, ApJL, 469, L33
Machida M., Nakamura K., Matsumoto R., 2004, PASJ, 56, 671
Makishima, K., Maejima, Y., Mitsuda, K., Bradt, H.V., Remillard, R. A., Tuohy, I. R., Hoshi, & R., Nakagawa, M. 1986, ApJ 308, 635
McClintock, J. E., Remillard, R. A. 2003, in Compact Stellar X-ray Sources, eds. Lewin W. H. G., & van der Klis, M., (Cambridge University Press, Cambridge), (astro-ph/0306213)
Miller, J. M., Raymond J., Fabian, A., Steeghs, D., Homan, J., Reynolds, C., van der Klis, M., & Wijnands, R. 2006, Nature, 441, 953
Mitsuda, K. et al. 1984, PASJ, 36, 741
Mitsuda, K. et al. 2006, PASJ, in press
Morrison, R., & McCammon, D. 1983, ApJ, 270, 119
Oosterbroek, T., Parmar, A. N., Kuulkers, E., Belloni, T., van der Klis, M., Frontera, F., & Santangelo, A. 1998, A&A, 340, 431
Parmar, A. N., Williams, O. R., Kuulkers, E., Angelini, L., & White, N. E. 1997, A&A, 319, 855
Parmar, A. N., Stella, L., & White, N. E. 1986, ApJ, 304, 664
Parmar, A. N., Angelini, L., & White, N. E. 1986, ApJ, 304, 664
Pereyra, N. A., Kallman, T. R., & Blondin, J. M. 2000, ApJ, 532, 563
Proga, D. 2000, ApJ, 538, 684
Proga, D. 2003, ApJ, 585, 406
Proga. D., & Kallman, T.R. 2002, ApJ, 565, 455
Proga, D., Stone, J. M., & Kallman, T. R. 2000, ApJ, 543, 686
Reynolds, C. S., & Wilms, J. 2000, ApJ, 533, 821
Serlemitsos, P., et al. 2006, PASJ, in press
Schattenburg, M. L., & Canizares, C. R. 1986, ApJ, 301, 759
Shakura, N. I., & Sunyaev, R.A. 1973, A&A, 24, 337
Sidoli, L., Oosterbroek, T., Parmar, A. N., & Lumb, D. 2001, A&A, 379, 540
Sidoli, L., Parmar, A. N., & Oosterbroek, T., Lumb, D. 2002, A&A, 385, 940
Takahashi, T., et al. 2006, PASJ, in press
Tanaka, Y., & Lewin, W. H. G. 1995, in X-ray Binaries, eds. W. H. G. Lewin, J. van Paradijs, and W. P. J. van den Heuvel (Cambridge University Press, Cambridge), p126
Tomsick, J. A., Lapshov, I., & Kaaret, P. 1998, ApJ, 494, 747
Toor, A., Seward, F. D. 1974, AJ, 79, 995
Trudolyubov, S. P., Borozdin, K. N., & Priedhorsky, W. C. 2001, MNRAS, 322, 309
Ueda, Y., Asai, K., Yamaoka, K., Dotani, T., & Inoue, H. 2001, ApJ, 556, L87
Ueda, Y., Inoue, H., Tanaka, Y., Ebisawa, K., Nagase, F., Kotani, & T., Gehrels, N. 1998, ApJ, 492, 782
Ueda, Y., Murakami, H., Yamaoka, K., Dotani, T., & Ebisawa, K. 2004, ApJ, 609, 325
Watarai, K., Fukue, J., Takeuchi, M., & Mineshige, S. 2000, PASJ, 52, 133
Woods, D. T., Klein, R. I., Castor, J. I., McKee, C. F., & Bell, J. B. 1996, ApJ, 461, 767
Yamaoka, K., Ueda, Y., Inoue, H., Nagase, F., Ebisawa, K., Kotani, T., Tanaka, & Y., Zhang, S. N. 2001, PASJ, 53, 179